Deep–Sea Research I 227 (2026) 104627

Contents lists available at ScienceDirect

Deep-Sea Research Part I

journal homepage: www.elsevier.com/locate/dsri

Antarctic Bottom Water contraction drives abyssal ocean warming along SAMBA-West line (34.5°S) in the Argentine basin

Daniel M.C. Santos [a,*], Tiago C. Biló [b,c], Dante C. Napolitano [d], Renellys C. Perez [e], Paulo S. Polito [a], Jonathan Gula [d,f], Shenfu Dong [e], Edmo J.D. Campos [a], Olga T. Sato [a]

[a] Instituto Oceanográfico da Universidade de São Paulo, Praça do Oceanográfico, 191, São Paulo, 05508-120, SP, Brazil
[b] School of Marine Sciences, University of Maine, College Avenue, 168, Orono, 04469, ME, USA
[c] Climate Change Institute, University of Maine, College Avenue, 168, Orono, 04469, ME, USA
[d] Univ. Brest, CNRS, IRD, Ifremer, Laboratoire d'Océanographie Physique et Spatiale (LOPS), IUEM, Rue Dumont d'Urville, Plouzané, 29280, BZH, France
[e] Atlantic Oceanographic and Meteorological Laboratory, National Oceanic and Atmospheric Administration, Rickenbacker Causeway, Miami, 4301, FL, USA
[f] Institut Universitaire de France, boulevard Saint-Michel, Paris, 75005, Île-de-France, France

ARTICLE INFO

Dataset link: https://www.aoml.noaa.gov/ftp/pub/phod/pub/SAM/hydrographic_data/, https://doi.org/10.5281/zenodo.11149277, https://doi.org/10.5281/zenodo.11108848, https://doi.org/10.5281/zenodo.11149213, https://doi.org/10.5281/zenodo.11148978, https://doi.org/10.1594/PANGAEA.915898, https://doi.org/10.1594/PANGAEA.915879, www.aoml.noaa.gov/phod/research/moc/samoc/sam/, https://doi.org/10.5281/zenodo.15365407, https://www.gebco.net/data_and_products/gridded_bathymetry_data/, https://doi.org/10.5281/zenodo.4948523

Keywords:
Abyssal warming
Antarctic bottom water (AABW)
Argentine basin
Deep ocean circulation
SAMBA-west array

ABSTRACT

We present an updated assessment of abyssal temperature trends in the Argentine Basin using expanded hydrographic and moored observations from the SAMBA-West line. The study addresses two main questions: (1) What is the spatial distribution of the abyssal warming along the SAMBA-West line? (2) What mechanisms drive the observed changes? Using output from a high-resolution numerical simulation, we first characterize how the abyssal flow near 34.5°S relates to the broader basin-scale circulation, providing context for interpreting the observations. Within this framework, we find that SAMBA-West is situated within a dynamically complex junction of deep boundary currents and recirculation pathways in the northwestern portion of the Argentine Basin. A coherent, statistically significant warming trend is found across most of the array and vertically throughout the AABW layer, primarily due to its vertical contraction, likely reflecting reduced formation or export of the AABW.

1. Introduction

Occupying up to 40% of the ocean volume below 4000 m (Johnson, 2008), the Antarctic Bottom Water (AABW) is the deepest, densest, and coldest water mass in the global ocean. This water mass is formed at four main sites around Antarctica: the Ross Sea, Weddell Sea, Prydz Bay, and Adelie Land Purkey et al. (2018). Its physical properties and formation rates result from the winter atmospheric forcing and mixing of colder and denser Antarctic Shelf Water with lighter and warmer Circumpolar Deep Water over the Antarctic slope (Orsi et al., 1999). Among the formation regions, the Weddell Sea is the primary source of the AABW that ventilates the Atlantic Ocean.

Approximately 90% of the AABW formed in the Weddell Sea enters the Atlantic Ocean (Solodoch et al., 2022), where it feeds the abyssal limb of the Atlantic Meridional Overturning Circulation (AMOC). In the Argentine Basin, AABW flows through the Malvinas Channels from the Georgia Basin (Georgi, 1981), circulates anticyclonically around the Zapiola Ridge, and exits mainly through deep channels located at its northern limit (Fig. 1; Smythe-Wright and Boswell, 1998; McDonagh et al., 2002). While its general pathways have been described (e.g., Coles et al., 1996), the AABW circulation within the basin remains mostly unknown.

In the Argentine Basin, the AABW is clearly distinguished from the overlying deep waters. The AABW core has a potential temperature of

* Corresponding author.
E-mail address: daniel.melo.santos@alumni.usp.br (D.M.C. Santos).

https://doi.org/10.1016/j.dsr.2025.104627
Received 31 May 2025; Received in revised form 17 November 2025; Accepted 19 November 2025
Available online 4 December 2025

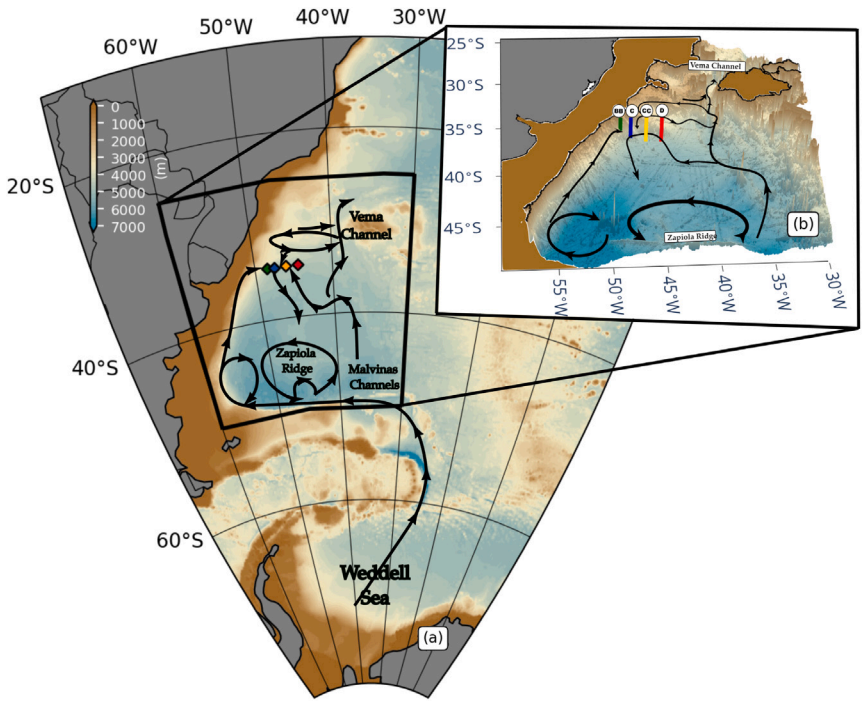

Fig. 1. (a): Schematic of the main pathways of the AABW (black arrows). Colored diamonds mark Site BB (green), Site C (blue), Site CC (orange), and Site D (red) of the SAMBA-West line. Background represents the bottom topography (m) from General Bathymetric Chart of the Oceans (GEBCO). (b): Zoom-in of the region outlined by the black box in panel (a).

about –0.10 °C and a salinity of about 34.67 (Valla et al., 2018). Its upper boundary, defined by $\gamma = 28.27$ kg m^{-3} (equivalently the $\theta = 0.0$ °C isotherm), marks the interface with the Lower Circumpolar Deep Water (LCDW), whose core properties are $\theta = 0.72$ °C and $S = 34.72$. The LCDW occupies the layer between AABW and the North Atlantic Deep Water (NADW), and its upper boundary ($\gamma = 28.10$ kg m^{-3}) closely follows the 2.0 °C isotherm.

The export of AABW from the Argentine Basin occurs mainly through the Vema Channel. This narrow passage is the principal conduit for AABW leaving the Argentine Basin and entering the Brazil Basin, making it a key chokepoint for abyssal volume transport (Hogg and Zenk, 1997; Hogg et al., 1982; Hogg and Owens, 1999; Zenk and Hogg, 1996; Morozov et al., 2018). Transport estimates range from 4.15 ± 1.27 Sv (Hogg et al., 1982) to 1.7 ± 1.1 Sv when accounting for compensating southward flow (McDonagh et al., 2002). This makes the Vema Channel not only a critical pathway for abyssal circulation but also a natural site for detecting long-term changes in AABW properties.

Indeed, evidence of such changes have accumulated over the past decades. Historical Conductivity–Temperature–Depth (CTD) profiles from 1972 to 2006 revealed a consistent warming of waters with potential temperature $\theta \leq 0.2$ °C (Zenk and Morozov, 2007). That warming persisted throughout 2010 (Zenk and Visbeck, 2013), reaching approximately 2.6 m°C yr^{-1} (m = 10^{-3}) by 2020 (Campos et al., 2021). Beyond the channel, the abyssal western South and tropical Atlantic have shown a basin-scale warming trend that varies meridionally (Johnson and Purkey, 2024), which appears to be linked to a long-term reduction in AABW volume (Purkey and Johnson, 2012; Zhou et al., 2023; Biló et al., 2024). The Argentine Basin reflects this broader pattern. Coles et al. (1996) reported a pronounced reduction in the densest AABW between 1980 and 1987, followed by an abyssal warming in 1989. Subsequent studies documented a general warming of waters deeper than 2000 m between 1989 and 2014 (Johnson et al., 2014), as well as a mean warming rate of about 2.1 m°C yr^{-1} for waters between 4500 and 6000 dbar (Johnson, 2022).

Despite a substantial body of work documenting abyssal warming trends across the Atlantic Ocean, direct estimates of the AABW transformation along its primary pathways remain limited. The western component of the South Atlantic MOC Basin-wide Array, hereafter SAMBA-West line, located in the northwestern Argentine Basin along 34.5°S (Fig. 2a), is strategically positioned to address this gap. Situated between the Brazil–Malvinas Confluence to the south and the Vema Channel to the north (Fig. 1), the array was designed to capture the full extent of the southward-flowing DWBC while also monitoring the spread of the AABW.

Monitoring deep and abyssal water-mass properties with sufficient accuracy to detect long-term changes is challenging, due to the small magnitude of temperature and salinity fluctuations at depth (e.g., Biló et al., 2024; Johnson and Purkey, 2024; Zhou et al., 2023). Moorings provide high temporal resolution but typically rely on single near-bottom instruments (e.g., Meinen et al., 2020; Campos et al., 2021), which can be strongly influenced by local processes. Hydrographic sections, in contrast, capture the full vertical structure and large-scale perspective of the water column but lack high-frequency temporal coverage. These complementary strengths and limitations underscore the value of integrated observing systems such as the SAMBA-West array, which combines high-frequency moored measurements with full-depth repeated hydrography.

Along the SAMBA-West line, Meinen et al. (2020) analyzed ocean-bottom temperature variability using temperature sensors integrated to pressure-equipped inverted echo sounders (PIES) together with a subset of CTD casts. With these two datasets, the authors reported mutually consistent indications of AABW warming from 2009 to 2019, with rates comparable to those reported for the Vema Channel and the broader Argentine Basin.

Building on these considerations and on the foundation established by Meinen et al. (2020), we integrate mooring and hydrographic observations to explore abyssal variability along the SAMBA-West line in greater detail. While the earlier study used only near-bottom points from the CTD casts, here we examine the full vertical extent of the profiles. We also extend the CTD time series from 2019 to 2022 and incorporate two new locations and one additional mooring site. Before assessing long-term temperature changes, we first characterize how the SAMBA-West line is embedded within the broader abyssal circulation

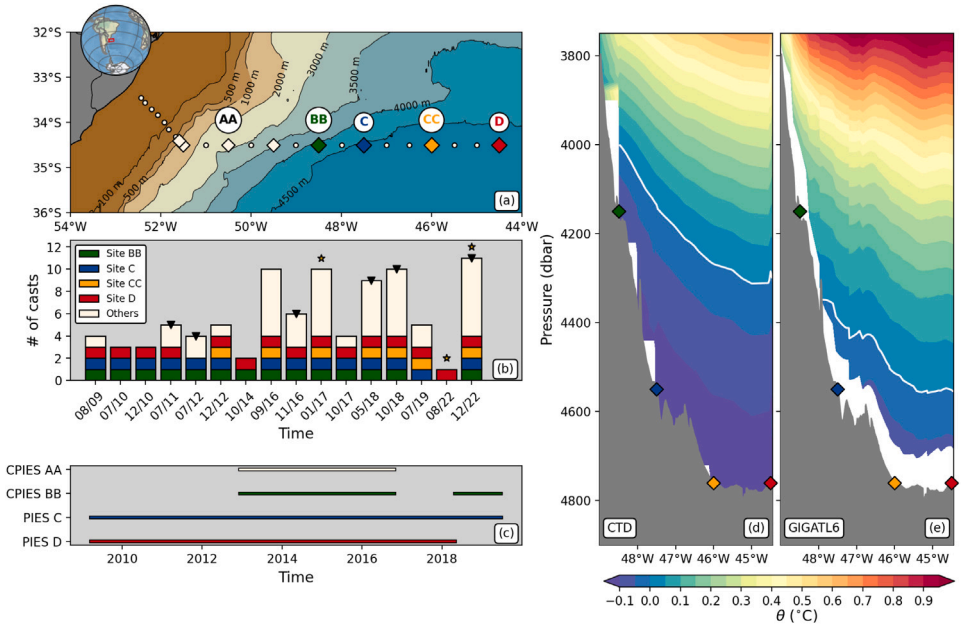

Fig. 2. Panel (a): Location of the moored instruments and hydrographic stations maintained at the SAMBA-West array. The colored shading represents the bathymetry of the study region from GEBCO. Diamonds mark CTD-PIES locations. Colored diamonds mark the PIES/CPIES locations: Site AA (white), Site BB (green), Site C (blue), Site CC (orange), and Site D (red). Circles mark CTD-only stations. Panel (b): Number of profiles that successfully captured AABW at Site BB (green), Site C (blue), Site CC (orange), Site D (red), and at other stations (white). Inverted triangles mark the cruises in which LADCP data were present, stars mark the MSM60, SAMBA19, and SAMBA20 cruises. Panel (c): Colored lines represent the time series of available PIES/CPIES data. Panel (d): Vertical section of time-averaged CTD θ. White line represents the upper limit of AABW (θ = 0.0 °C). Green, blue, and red diamonds mark sites BB, C, CC, and D locations, respectively. Panel (e): Same as (d), but for the GIGATL6 numerical simulation output.

using a high-resolution regional numerical simulation; this provides essential spatial context for interpreting the observations. We then address two scientific questions: (1) What is the spatial distribution of the abyssal warming along the SAMBA-West line? (2) What mechanisms drive the observed changes?

2. Data

2.1. Observations

Our analysis is focused on temperature and velocity observations along the SAMBA-West line (Fig. 2a). Temperature data were collected from temperature sensors housed inside PIES and PIES equipped with single-point acoustic current meters (CPIES) as well as from CTD profiles. Velocity measurements were obtained from Lowered Acoustic Doppler Current Profiler (LADCP), attached to the CTD frame as well as from the CPIES. In addition, salinity profiles obtained from CTD casts were used as a supporting variable to help decompose the observed temperature trends into heave and spiciness components.

The CTD data come from a series of repeated hydrographic cruises conducted along the SAMBA-West line near 34.5°S supporting long-term monitoring efforts in the region. Those surveys have been conducted with quasi-annual frequency, totaling 15 cruises since 2009 (Fig. 2b). In addition to the repeated section, we also analyzed data from a trans-basin cruise conducted aboard the R/V *Maria S. Merian* in January 2017 (MSM60; Karstensen et al., 2019) that followed the same latitude as the SAMBA-West line, for a total of 16 cruises.

The number of CTD casts sampling down to the AABW varied among cruises, ranging from 1 to 11 stations per cruise (Fig. 2b). For this study, we selected the four locations with the largest number of casts: 48.5°W (14 profiles), 47.5°W (14 profiles), 46°W (7 profiles), and 44.5°W (15 profiles). These stations correspond to Sites BB, C, CC, and D, respectively, as commonly referenced in the literature and shown in Fig. 2 (Chidichimo et al., 2021, 2023; Valla et al., 2018, 2019; Meinen et al., 2017, 2020). All four locations lie within the deep or abyssal portion of the basin, with depths of 4165 m (Site BB), 4565 m (Site C), 4750 m (Site CC), and 4780 m (Site D). LADCP velocity data are available from six cruises, with the corresponding years indicated in Fig. 2b. Both CTD and LADCP casts typically extend from the surface to within approximately 10–20 m of the seafloor, and the maximum sampled pressure for each cast is provided in Supplementary Figure S1.

The historical SAMBA dataset spans August 2009 to July 2019 and includes CTD measurements at Sites C and D used in Meinen et al. (2020). To extend this record, we incorporate CTD data from the MSM60 trans-basin cruise in January 2017 (Karstensen et al., 2019) and from two recent SAMBA-West cruises conducted in August and December 2022 (SAMBA19 and SAMBA20), which update the CTD time series at Sites C and D to 2022. We also expand the analysis to two additional CTD sites, BB and CC, and extend the LADCP analysis of Valla et al. (2019) through 2022. Details of the CTD and LADCP instrumentation and processing are provided in the Supplementary Information.

The PIES and CPIES instruments used in this study were deployed in five locations along the SAMBA-West line: PIES at Sites C and D, and CPIES at Sites AA (–50.5°W), BB, and CC. All instruments were moored about 1 m above the seafloor and collected data during different portions of the 2009–2019 period (Fig. 2c). Although Site CC was equipped with a CPIES, its temperature record could not be calibrated due to the lack of CTD casts at this location, and its velocity record was unusable due to an instrument malfunction; therefore, Site CC was excluded from the analysis. Site AA is too shallow to monitor AABW, but velocity measurements at this site are used for model-validation purposes. Sites C and D were already included in the analysis of Meinen et al. (2020), while Site BB is analyzed here for the first time. All instruments recorded hourly data.

2.2. Numerical model

Complementary to the *in situ* observations, we incorporate output from a high-resolution ocean general circulation model (GIGATL6; cf.

Table 1
Comparison of velocity statistics between CPIES and GIGATL6 (1-hour average)

Variable	Dataset	Statistic	AA	BB	C	CC	D
u [m s^{-1}]	CPIES	Mean	0.015	0.055			
		Std	0.064	0.150			
	GIGATL6	Mean	0.020	0.036	0.008	−0.007	−0.013
		Std	0.062	0.137	0.111	0.064	0.061
v [m s^{-1}]	CPIES	Mean	0.010	0.005			
		Std	0.054	0.047			
	GIGATL6	Mean	0.013	0.014	0.023	0.012	0.003
		Std	0.046	0.043	0.052	0.048	0.041
Angle [°]	CPIES	Mean	31.89	5.07			
	GIGATL6	Mean	33.10	20.53	69.80	119.80	166.29

Gula et al., 2021) to gain insight into the regional mean flow and fill the spatial gaps between observation sites. We examined 5-day averages of model velocity and θ from March 2005 to January 2012 (e.g., Qu et al., 2021; Ruan et al., 2021; Tagliabue et al., 2022; Vic et al., 2022; Schubert et al., 2025). The horizontal velocity outputs were further used to compute stream function (ψ) fields following the methodology of Li et al. (2006), providing a comprehensive picture of the horizontal circulation patterns at a specific depth.

GIGATL6 is based on the Coastal and Regional Ocean COmmunity model (CROCO; Auclair et al., 2025) developed upon the Regional Oceanic Modeling System (ROMS; Shchepetkin and McWilliams, 2005). GIGATL6 spans the Atlantic Ocean at a nominal horizontal resolution of 6 km with 50 vertical levels that follow the seafloor topography, sourced from the Global Bathymetry and Elevation Data at 30 Arc Seconds Resolution (Becker et al., 2009). The model configuration includes initial and boundary conditions from the Simple Ocean Data Assimilation (SODA) project version 2.2.4 (Carton and Giese, 2008), atmospheric forcing from the hourly Climate Forecast System Reanalysis (Saha et al., 2010), a k-ϵ turbulence closure scheme for vertical mixing parameterization (Umlauf and Burchard, 2003), and tidal forcing derived from TPXO7.2 and GOT99.2b (Ray, 1999).

To assess the model's reliability, we compared the mean and standard deviation of the GIGATL6 velocities with CPIES measurements from 2012 to 2016 at sites AA and BB. CPIES instruments provide hourly velocity records, allowing a robust comparison. Site BB is the primary focus, while Site AA serves as an additional validation point. Hourly GIGATL6 velocities were used for consistency, and statistics were computed over 2008–2011 at the deepest model level.

Table 1 summarizes the key statistics of the horizontal velocity components. The comparison shows that GIGATL6 captures the main flow features at both validation sites, reproducing the overall magnitude, direction, and variability of the observed currents. The difference in the mean flow direction at Site BB is likely related to bathymetry effects in the model, where the isobaths have a local disagreement in their positions compared to the observations (Supplementary Figure S2). Despite this difference, the general agreement provides confidence that GIGATL6 can be used to complement the *in situ* observations, filling spatial gaps and enabling a more complete analysis of the near-bottom circulation patterns. Detailed interpretation and discussion of the velocities from GIGATL6 and LADCP measurements collected during the repeated ship transects are presented in Section 3.

Although the simulation dynamics are consistent with available observations, it is important to note that GIGATL6 was not configured specifically for comparison with SAMBA-West measurements. Consequently, while the model reproduces the large-scale flow patterns, it systematically overestimates abyssal temperatures relative to the observed profiles, a well-known limitation of state-of-the-art Ocean General Circulation Models (Heuzé, 2020). This warm bias is reflected in the isotherm defining the upper limit of the AABW, which lies approximately 350 m deeper in the model than in the observations (Fig. 2d, e). As a result, Site BB lies within the AABW layer in the observations but above it in the model. To account for this discrepancy, we subtracted the time-mean GIGATL6 θ field from the time-mean *in situ* field and removed this offset from the model temperatures (see Supplementary Information).

As part of ongoing efforts to improve the representation of abyssal waters in Ocean General Circulation Models, we analyzed several ocean climatology and reanalysis products and found similarly large temperature biases in the abyss, with deviations of up to about 0.4 °C. This suggests that the warm biases in GIGATL6 likely originate from biases already present in the SODA initial and boundary conditions (not shown).

3. SAMBA-West connectivity

In the Argentine Basin, Coles et al. (1996) proposed several circulation pathways for AABW using a thermal wind proxy, providing a schematic circulation in which the AABW enters the basin through the Malvinas Channels. From there, part of the flow follows isobaths westward, while another portion flows directly northward to form an anticyclonic flow around the Zapiola Ridge. The westward branch subsequently turns northward, where it splits: one segment continues to flow northeastwards, ultimately contributing to northward AABW export through Vema Channel, while the other recirculates cyclonically to the south, reaching the Zapiola gyre (see Figure 3 of Coles et al., 1996).

Overall, the schematic circulation proposed by Coles et al. (1996) closely aligns with the mean abyssal flow pattern reproduced by GIGATL6 (Fig. 3a). The model captures key features, including the anticyclonic flow around the Zapiola Ridge, the northward flow along the western portion of the basin and the cyclonic recirculation to the south. In addition to this, another interesting feature is well reproduced by the model: the southward, anticyclonic, flow centered at 47–46°W along the SAMBA-West line (Valla et al., 2019). This feature lies between Sites C and CC (Fig. 3b), is likely steered by local topography, and may explain the observed southward flow of AABW at this location.

The model also agrees with previous analysis of the SAMBA-West velocity structure. Valla et al. (2019) found that west of ~48 °W, the abyssal flow is largely influenced by the southward-flowing DWBC. East of this longitude, the flow becomes more complex, with the presence of alternating northward and southward jets (see Figure 1 of Valla et al., 2019), which is well reproduced by the model, with both observations and model capturing the zonal and meridional velocity inversions along the array. The barotropic nature of the flow is also realistically represented. Key features such as the Deep Western Boundary Current (DWBC) are clearly resolved, underscoring the model's ability to capture the main abyssal circulation patterns (see Fig. 3c-f). Nevertheless, some discrepancies between GIGATL6 output and CPIES/LADCP measurements are expected, given the limited temporal and spatial coverage of the observations compared with the model's continuous output.

Some unique features are also reproduced by the model. The most notable being the closed circulation in the northwestern portion of the Argentine Basin, where the ψ field is mainly positive (Fig. 3a). In this region, waters reaching Site D originate mainly from the basin interior. After crossing this site, they turn toward Site CC (Fig. 3b) and subsequently feed the southward flow described by Valla et al. (2019). Site C appears to be located at the confluence of waters arriving from the west and from the north, associated with the large anticyclonic circulation north of the SAMBA-West line, before turning southward. The model also shows that most of the waters that cross the Vema Channel come from the interior of the basin, from a main branch that also feeds the western portion of the SAMBA-West line. It has a smaller contribution from an east flowing branch, which is part of the recirculation cell that interacts with the stations of the SAMBA-West array from the north (Fig. 3b).

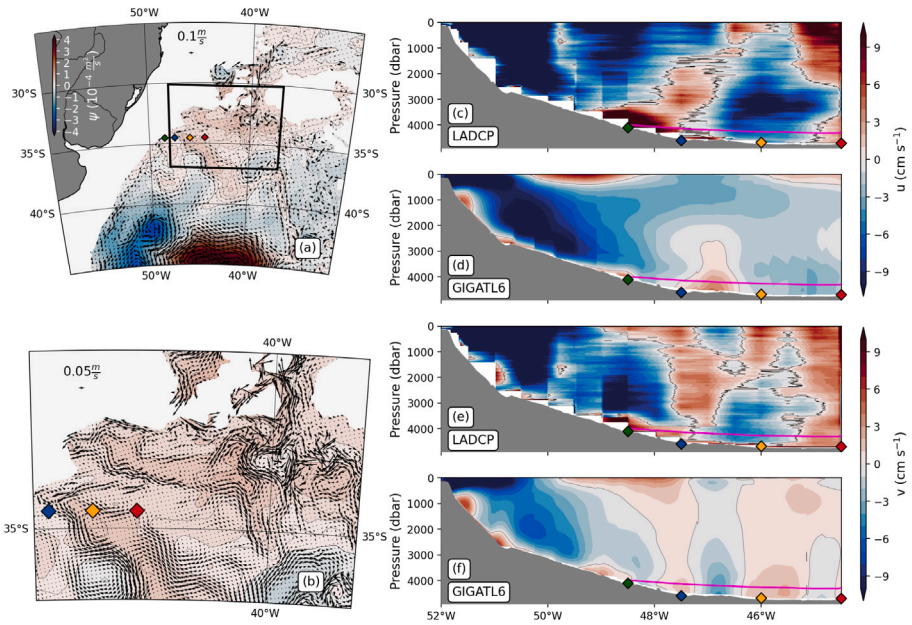

Fig. 3. Panel (a): Time-averaged horizontal velocity vectors (black arrows) and streamfunction field (contours and colored shading) from the deepest layer of the GIGATL6 simulation, masked at 3800 dbar. Panel (b): Zoom-in of the region outlined by the black box in panel (a). Panel (c): Time-averaged zonal velocity from *in situ* observations along 34.5°S. Panel (d): Time-averaged zonal velocity from the GIGATL6 simulation along 34.5°S (red shading indicates eastward velocity, and blue indicates westward velocity). Panel (e): Time-averaged meridional velocity from *in situ* observations along 34.5°S. Panel (f): Time-averaged meridional velocity from the GIGATL6 simulation along 34.5°S (red indicates northward velocity and blue indicates southward velocity). Diamonds indicate PIES deployment sites: green for Site BB, blue for Site C, orange for Site CC, and red for Site D. Magenta thick line represents the upper limit of AABW ($\theta = 0.0$ °C).

Site BB, however, lies at the edge of this closed recirculation, a unique location near the limit of the AABW, where the 0 °C isotherm intersects the bathymetry (Fig. 2d), and waters appear to come from the southwestern portion of the basin. Dynamically it shows extreme variability: the standard deviation of the model velocity components is several times larger than their means, with ratios of 3.8 (u) and 3.0 (v). Site C shows a similar pattern, with ratios of 13.0 (u) and 2.2 (v). The velocities components at BB are also highly anisotropic between each other: the mean of u is 2.5 times larger than the mean of v, while the standard deviation of u is 3.1 times larger than that of v. In contrast, at Site C the mean of u is 2.8 times smaller than the mean of v, but its standard deviation is 2.1 times larger. Such variability at BB has been attributed to the passage of westward-propagating eddies consistent with Rossby wave–like features (Meinen et al., 2017), while the variability at Site C may be related to the anticyclonic cell placed north of it.

The GIGATL6 simulation, together with *in situ* measurements (Fig. 3c–f), clarifies the integration between the SAMBA-West transect and the broader flow pattern in the Argentine Basin, including its connection to the Vema Channel. The model supports earlier findings (McDonagh et al., 2002; Coles et al., 1996), while also brings new interpretations of the main pathways of the AABW. The highly intricate bathymetry of the region (Fig. 1b) appears to play a central role in shaping abyssal circulation. Dynamically, sites BB and C are unique spots characterized by a velocity variability that far exceeds the mean flow, probably linked to the DWBC (Site BB) and to the anticyclonic circulation north of it (Site C). However, sites C and D seem to be more related to each other and to the interior circulation of the basin. Although these advances refine the description of the mean abyssal circulation, a dedicated study is still required to fully understand the dynamics of the deep and abyssal circulation along the SAMBA-West line.

4. Abyssal warming

The following revisits and expands (Meinen et al., 2020) by extending the CTD record to 2022 and increasing the spatial coverage of CTD/PIES sites along the SAMBA-West line, enabling a more detailed assessment of abyssal temperature trends. Here we use *in situ* temperature from the PIES instruments, since salinity measurements are not available to compute potential temperature. For consistency, we therefore compare these with the equivalent *in situ* temperatures from the CTD casts.

Although the PIES temperature records are calibrated using concurrent near-bottom CTD measurements and thus are not fully independent (see Supplementary Information), the comparison between the two datasets still supports the reliability of the CTD-derived trends (Table 2). The PIES data, due to their high temporal resolution, provide time series with greater degrees of freedom, resulting in a more statistically robust 95% Confidence Interval (CI). This reinforces the validity of the CTD-derived trends, despite their lower temporal resolution and relatively smaller number of data-points.

Hence, one important caveat is that CTD-based trend analysis is limited by relatively sparse temporal sampling. According to Meinen et al. (2012), achieving a temperature trend accuracy of 0.01 °C per decade (therefore approximately 0.001 °C per year) at the 95% confidence level requires sampling approximately once per year or more frequently. The hydrographic cruises used in this study satisfy this requirement, but our sampling frequency is at the threshold of this criterion. As such, uncertainties of this magnitude are expected and should be taken into account when interpreting the results, particularly at Site BB.

Before presenting the CTD-derived trends, the dataset was subjected to additional quality control (see Supplementary Information). Outliers were removed using a threshold of 1.5 times the interquartile range (IQR), which led to the exclusion of Site BB data from the October 2017 cruise (SAMBA14). At this location, the CPIES record has a major gap between 2017 and 2018 (Fig. 2c). Hence, to estimate its temperature trend, we calculated the difference between the mean values of the two uninterrupted segments of the time series, considering only periods with active instrument records.

The inclusion of the 2022 cruises confirms that the warming trend of about 0.002 °C per year previously identified at sites C and D (Meinen

Table 2
Locations of the PIES Moorings and CTD Casts, along with basic statistics of the *in situ* temperatures from 2009 to 2019.

	Equipment	Latitude (°S)	Longitude (°W)	Mean (°C)	Standard deviation (°C)	Trend (°C per year)	CI 95% (°C per year)
Site BB	PIES	34.5	48.5	0.1939	0.0193	0.0048[a]	0.0063
	CTD	34.5	48.5	0.2023	0.0181	−0.0008	0.0027
Site C	PIES	34.5	47.5	0.2229	0.0078	0.0022	0.0015
	CTD	34.5	47.5	0.2234	0.0089	0.0021	0.0012
Site CC	PIES	–	–	–	–	–	–
	CTD	34.5	46.0	0.2469	0.0065	0.0022	0.0018
Site D	PIES	34.5	44.5	0.2398	0.0063	0.0019	0.0014
	CTD	34.5	44.5	0.2472	0.0082	0.0019	0.0011

[a] Defined using the difference of the mean temperature from two deployment periods.

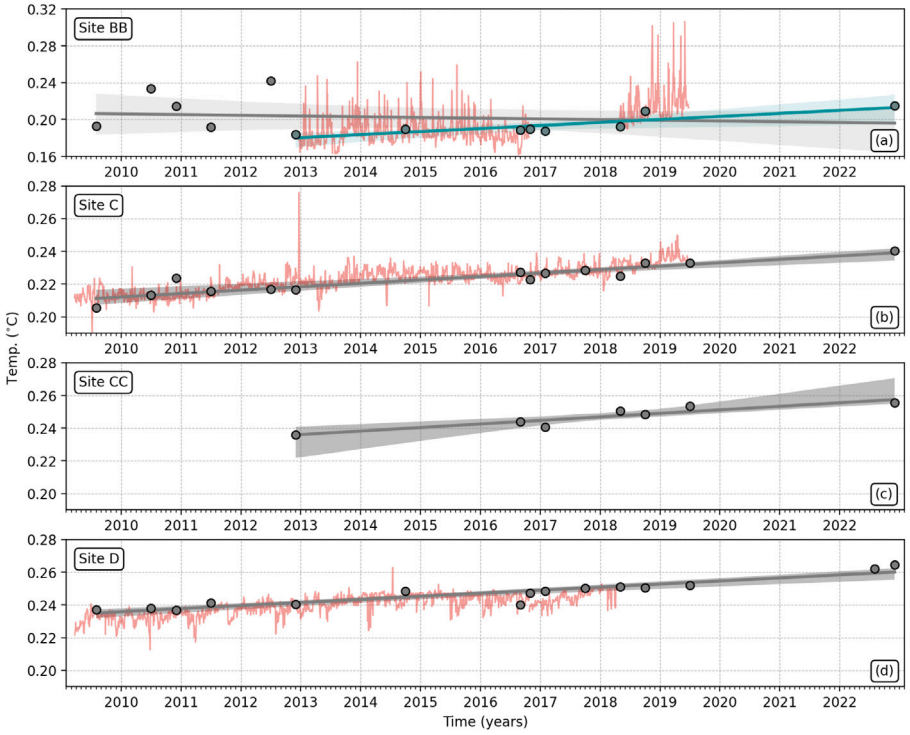

Fig. 4. *In situ* temperature records from PIES (red lines) alongside temperatures from the deepest bin of each CTD cast (gray circles) at Site BB (panel a), Site C (panel b), Site CC (panel c), and Site D (panel d). Gray lines indicate the linear regression of the CTD data, with shaded areas representing the 95% confidence intervals. The teal line in panel (a) represents the linear regression of the CTD data beginning at 2013, with the shaded area representing the 95% confidence interval.

et al., 2020) persists beyond 2019 (Fig. 4 and Table 2) and remains significantly different from zero with 95% confidence. A similar positive and significant trend of 0.0022 °C per year is now evident at Site CC, spanning the period from 2013 to 2022. In contrast, based on CTD measurements collected from 2009–2022, Site BB shows a slight overall cooling that is not significantly different from zero. However, if the analysis is restricted to the CTD record beginning in 2013, it indicates a significant warming trend of 0.0033 °C per year, consistent with the PIES trend during this time period.

Regardless of this agreement, the PIES temperature trend at Site BB is not significantly different from zero (Table 2). This likely arises because Site BB lies on the edge of the AABW domain, where interactions with adjacent water masses introduces variability. At this location, the standard deviation of the CTD temperature record is roughly 20 times larger than the magnitude of its trend, and for the PIES record, the standard deviation is approximately 4 times larger than the magnitude of its trend, which helps explain the lack of statistical significance. In contrast, the other sites, which are more centrally located within the AABW layer experience lower background variability and exhibit robust and statistically significant warming trends (Table 2).

Overall, the warming trend along the SAMBA-West line is robust and consistent at all sites except BB. This is particularly noteworthy at Site CC, which, despite having roughly half as many CTD data points as the other sites, still shows a comparable warming signal, despite having fewer degrees of freedom. These trends are consistent with those observed in other regions of the Argentine Basin such as in the southeast portion of the Argentine Basin with rates of 2–4 m°C yr^{-1} (Johnson et al., 2014) and within the Vema Channel with rates of about 2.6 m°C yr^{-1} (Campos et al., 2021), further reinforcing the connection between the western portion of the SAMBA-West line, the Vema Channel and the rest regions of the Argentine Basin.

To explore the vertical structure of these changes, we next analyze potential temperature (θ) derived from the CTD profiles. The θ trends along pressure levels are not statistically significant within the LCDW, that is, above the dashed lines in Fig. 5a, c, e, g. Below this layer, however, the AABW exhibits a general warming (Fig. 5b, d, f, h), with trends significantly different from zero at the deepest portion of the profiles at sites C and D. At Site CC, the deepest portion of the profile also shows significant warming, but the confidence intervals at this location are wider than at other sites with the boundaries of the gray shaded region nearly overlapping with the 0.0 m°C yr^{-1} line, likely due

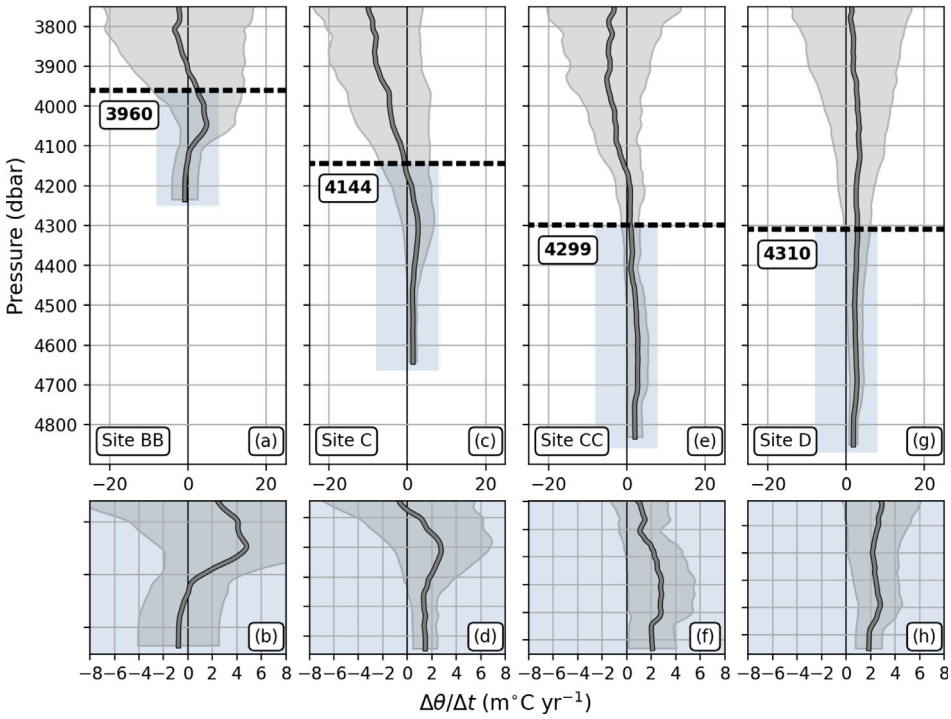

Fig. 5. Potential temperature (θ) trends as a function of pressure (p) at Site BB (panel a), Site C (panel c), Site CC (panel e), and Site D (panel g). The dashed line indicates the mean pressure interface between the LCDW and the AABW, with its values annotated below it. Gray shading indicates the 95% confidence intervals. Blue boxes highlight the zoomed-in regions shown in panels (b), (d), (f), and (h), corresponding to panels (a), (c), (e), and (g), respectively.

to fewer degrees of freedom. Interestingly, Site BB shows a reversal of the trend in the deepest part of the AABW. Despite having a comparable number of data points to sites C and D, the CTD trends at Site BB are not statistically significant at any depth in the LCDW and AABW layer, which limits our ability to draw firm conclusions about the temperature changes at that location.

In summary, the θ profiles at sites C, CC, and D consistently show significant warming in the bottommost AABW layers, reinforcing the view of a basin-scale warming signal that extends across the Argentine and Brazil basins (Campos et al., 2021; Meinen et al., 2020; Johnson and Purkey, 2024). This spatial coherence strengthens confidence that the observed changes reflect large-scale processes rather than local variability. In contrast, Site BB emerges as an exception: despite comparable sampling size, its record lacks statistically significant trends and even suggests localized cooling in the deepest layer from 2009 to 2022 (Fig. 5b). This probably reflects its boundary position between distinct water masses, where the high variability obscures long-term signals. Together, these results highlight a robust warming of the AABW in the northwestern Argentine Basin and the importance of observing and characterizing site-specific variability when interpreting regional abyssal trends.

5. Warming drivers

We decompose the θ trends along pressure levels into spiciness and heave components (Bindoff and Mcdougall, 1994):

$$\left.\frac{\Delta\theta}{\Delta t}\right|_p \approx \left.\frac{\Delta\theta}{\Delta t}\right|_\gamma - \left.\frac{\Delta p}{\Delta t}\right|_\gamma \left(\frac{\partial\theta}{\partial p}\right), \quad (1)$$

where $|_p$ denotes changes along isobaric levels and $|_\gamma$ denotes changes along isopycnal levels. While spiciness [first term in the RHS of (1)] represents a change in θ and S upon a fixed isopycnal surface, heave [second term in the RHS of (1)] represents vertical migration of isopycnals (Häkkinen et al., 2016), where the term $\left(\frac{\partial\theta}{\partial p}\right)$ is the time averaged background thermal gradient. To define the γ levels, we create an evenly spaced vertical grid of γ for each location with resolution of 0.0005 kg m^{-3}. Then, we linearly interpolated p and θ profiles onto the γ grid. Finally, we quantified its trends as the slope of a linear least-square fit.

A key limitation of (1) is its dependency on salinity changes, which are not statistically significant at the 95% confidence level given the small sample size and measurement uncertainty (Supplementary Figure S4). Nevertheless, the sum of the heave and spiciness components closely reproduces the observed θ trends (Fig. 6, yellow and gray lines), lending confidence to the decomposition of the temperature signal into heave and spiciness contributions.

Also, the accuracy of this approximation is strongly dependent on the number of available data points. At all sites, data loss due to vertical interpolation affects the reconstruction of the θ trend, particularly in the deepest portions of the profiles, where downward motions of near bottom isopycnals force them out of the observed region at certain times (see dotted lines in Fig. 6). Compared with the other sites, Site BB shows the weakest correspondence, likely due to both significant data loss and elevated temperature variability, which can affect the background thermal gradient $\left(\frac{\partial\theta}{\partial p}\right)$ and reduce the accuracy of the decomposition.

Heave is the primary driver of positive AABW temperature changes along the SAMBA-West line. At most locations, downward displacement of isopycnals (i.e., positive heave) appears to overcome the freshening effect (i.e., negative spiciness) in setting the observed warming trends within the AABW. Although the overall pattern is clear, the relative contributions of spiciness and heave vary between different water masses and sites.

At Site BB (Fig. 6a), the θ trend is negative throughout most of the LCDW layer, where heave oscillates between small negative and positive values and spiciness exhibits larger magnitudes. This results in a predominantly negative trend extending from above 3750 dbar to approximately 3900 dbar. Below this pressure level and as the magnitude of heave increases with depth, the θ trends begin to show positive values as well. Specifically, the upper portion of the AABW

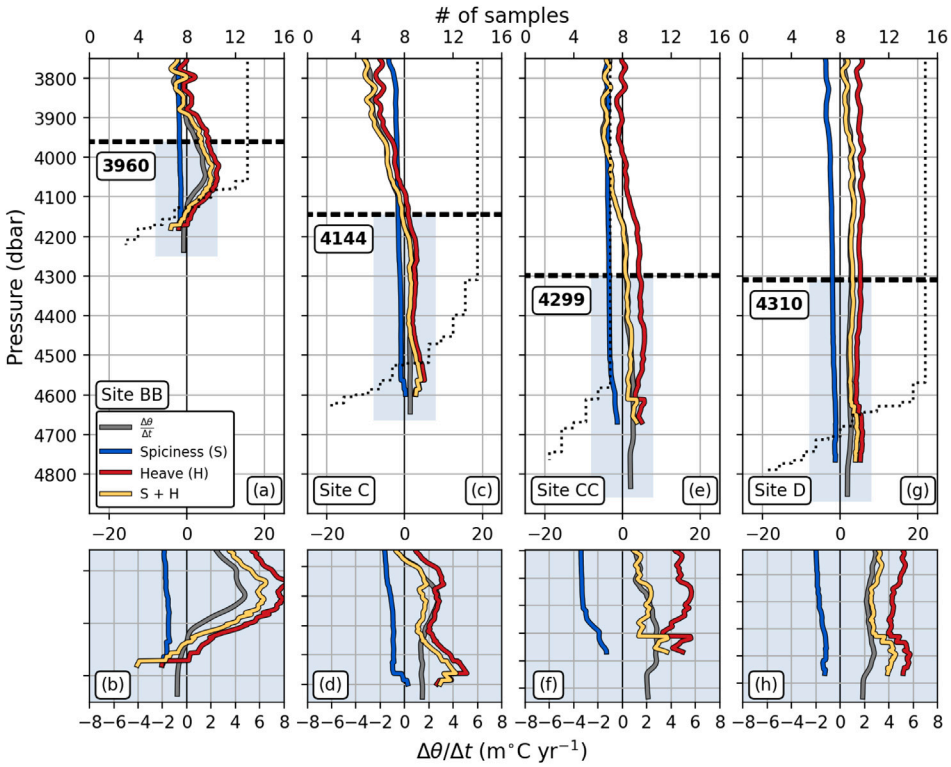

Fig. 6. Panel (a): Potential temperature (θ) trend (gray line) and its approximation (yellow line), decomposed into heave (red) and spiciness (blue) components at Site BB. The dashed line indicates the mean pressure interface between the LCDW and the AABW, with its values annotated below it. The dotted line shows the number of data points used in the calculation. Panel (c): Same as (a), but for Site C. Panel (e): Same as (a), but for Site CC. Panel (g): Same as (a), but for Site D. Panels (b), (d), (f), and (h) show zoomed-in views of the blue-boxed regions from panels (a), (c), (e), and (g), respectively. Trends calculated with less than four sample points are masked.

(Fig. 6b) shows a warming trend, while the deeper layers exhibit cooling, driven by the decrease in the magnitude of the heave component below 4050 dbar.

At Site C (Fig. 6c), within the portion of the profile typically associated with the LCDW, both the spiciness and heave components contribute to a cooling trend, acting in the same direction. This cooling is primarily driven by the heave component, which dominates the θ trend. Below these depths (at approximately 4100 dbar), heave becomes increasingly positive and in consequence the trends shift to positive, leading to a warming signal in the depths occupied by the AABW (Fig. 6d).

At Site CC (Fig. 6e), the overall pattern within the LCDW layer shows θ trends predominantly negative. Similar to Site BB, this negative trend is driven by both spiciness and heave components, with heave fluctuating between small negative and positive values and spiciness dominating the cooling trend. As heave increases in magnitude with depth, the θ trend shifts to positive values near 4150 dbar reaching a peak near 4600 dbar with heave emerging as the dominant contributor to the observed θ changes in the AABW layer (Fig. 6f).

At Site D (Fig. 6g), the trend components exhibit a distinct relation compared to those at sites BB, C, and CC above 4150 dbar, within the LCDW layer. Heave and spiciness components act in opposite directions: heave contributes to warming, while spiciness induces cooling. In contrast, θ trends in the AABW layer (Fig. 6h) follow the pattern observed at the other sites, with heave largely driving the warming trend.

6. AABW contraction

To better visualize the vertical displacement of isotherms, we analyzed trends in isotherm depth above the bottom (h) as a function of θ. Before calculating these trends, we generated an evenly spaced vertical θ grid for each site, considering the maximum and minimum θ values of each time series, with a resolution of 0.01 °C. We then linearly interpolated the corresponding h profiles onto these θ grids. Finally, the h trend at each θ level (Fig. 7 a, b, c, and d) was estimated by computing the slope via linear least-squares fit.

The analysis of the h trends provides insight not only into temporal changes at specific θ levels but also into the shifts among waters from one θ class to another. As outlined by Johnson et al. (2014), layer thickness changes can be inferred from how h trends vary with θ. If the trends tend toward negative values of $\frac{\Delta h}{\Delta t}$ as θ increases, the layer is thinning. If the trends tend toward positive values of $\frac{\Delta h}{\Delta t}$ as θ increases , the layer is thickening. When isotherm depth remains constant with respect to temperature, the layer thickness is unchanged.

At Site BB (Fig. 7a), the profile shows no significant observed trends throughout most of the water column, with fluctuations that on average produce a near-zero mean trend. At sites C and CC (Fig. 7b and c), waters within approximately 0.0 °C and 1.0 °C, and 0.1 °C and 1.0 °C, respectively, show positive h trends, although these are not significant at the 95% confidence level. At Site C, this upward movement is relatively uniform across the θ classes, whereas Site CC exhibits greater variability. Below 0.0 °C, both sites display negative trends: waters between roughly −0.15°C and 0.0 °C are generally descending at a decreasing rate as θ increases. The maximum rate of descent occurs at −0.15 °C with values of about −10 m yr^{-1} at Site C and −15 m yr^{-1} at Site CC. For waters colder than −0.15°C, the pattern reverses, with waters generally descending at an increasing rate as θ increases.

At Site D (Fig. 7d), negative h trends are observed throughout the entire profile, but they are only significant with 95% confidence in the AABW layer. This pattern contrasts with sites C and CC within the temperature range between approximately 0.0 °C and 1.0 °C, where those sites exhibited positive trends. However, as temperature decreases, the patterns at Site D start to resemble those observed at

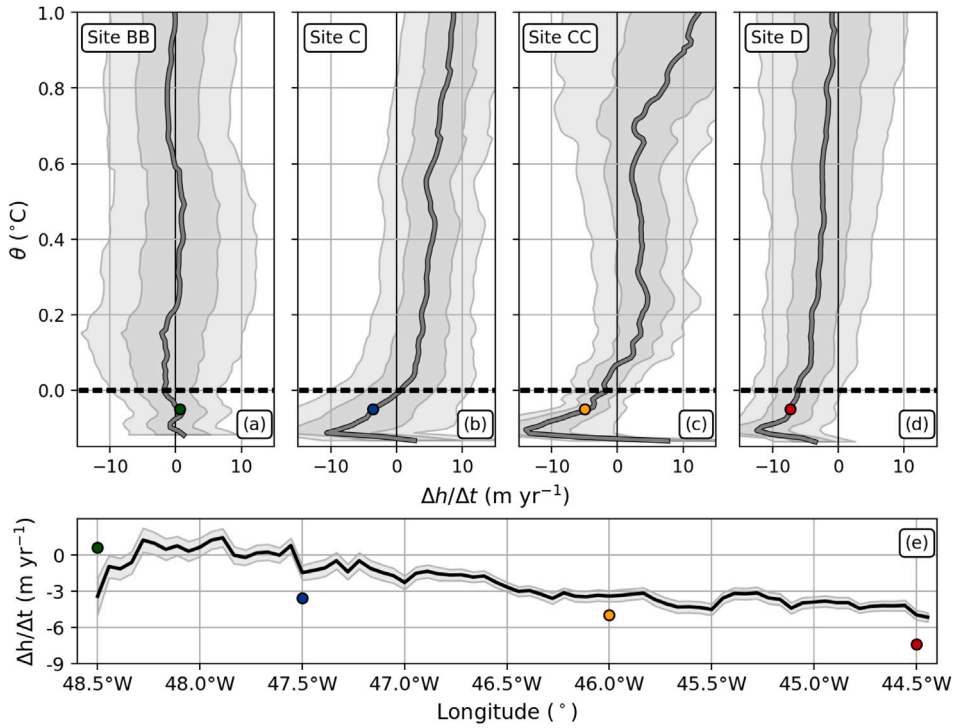

Fig. 7. Trends in isotherm depth above the bottom (h) as a function of potential temperature (θ) at Site BB (panel a), Site C (panel b), Site CC (panel c), and Site D (panel d), from *in situ* data. Shaded areas indicate the 68% and 95% confidence intervals. Colored circles mark the trend of the −0.05 °C isotherm. Horizontal dashed line marks the boundary between the AABW and LCDW layers (θ = 0.0 °C). Panel (e): shows the trend of the −0.05 °C isotherm along 34.5°S. Colored circles represent *in situ* data, the bold black line shows the trend from the GIGATL6 simulation output, the shaded area between gray lines indicates the 95% confidence interval.

sites C and CC. Below 0.0 °C, waters between roughly −0.15 °C and 0.0 °C are generally descending at a decreasing rate as θ increases. It has a maximum rate of descent of about −12 m yr^{-1} at −0.15 °C. For waters colder than approximately −0.15 °C, waters generally descend at an increasing rate as θ increases.

We selected the isotherm of −0.05 °C as a case study and compared the h trends from *in situ* observations and model simulations (Fig. 7e). The model results corroborate the *in situ* data, showing two distinct regions along the SAMBA-West line: (1) the western portion with near-zero h trends, reaching slightly positive values around 48°W and (2) the eastern portion with mainly negative trends. Importantly, we highlight that the utilized simulation covers a relatively short time period, which limits the robustness of comparisons with the observations.

Thus, the AABW layer (θ < 0.0 °C) in the sites C, CC, and D appear to be interconnected, exhibiting similar trends along the line. These sites also have a similar pattern of h trends across different temperature classes, which is characterized by a "V-shape" in the profiles (Fig. 7b, c, and d). These changes suggest a thinning of the cold AABW layers, which is partially offset by a thickening of its warm layers, although the layer as a whole contracts. Only Site D has significant trends with 95%, however we note that the "V-shape" pattern present in these sites closely resembles those reported by Johnson et al. (2014) in the southern Argentine Basin. This similarity supports the robustness of the observed results and indicates potential regional connectivity among these sites and the rest of the basin.

The trends within the assessed portion of the LCDW layer (0.0 °C < θ < 1.0 °C) are different from the AABW layer. They show little to no sign reversal with depth at all sites. This consonance suggests that changes in layer thickness within this part of the LCDW are not balanced across different temperature ranges, with the entire assessed portion tending to lose or gain thickness uniformly.

Hence, AABW expands uniquely at Site BB but contracts at Sites C, CC, and D. The expansion at Site BB is linked to heave: the θ trend there (Fig. 6a) reverses from warming to cooling near the bottom while spiciness remains negative, indicating cooling driven by heave and a local thickening of AABW. At Site D, in contrast, h remains negative throughout the profile because the heave contribution is consistently positive, sustaining contraction of the AABW layer. At Sites C and CC, the heave term changes sign with depth, which drives a transition in h trends from positive values in the upper portion to negative values deeper down. Together, these cases highlight the distinct ways in which heave controls AABW variability across the section.

The overall dominant signal across the SAMBA-West line is one of contraction (negative h trend). This contraction is consistent with the broader hypothesis that weakened production of dense waters in the Weddell Sea has slowed the abyssal cell of the AMOC. Abrahamsen et al. (2019) showed that reductions in the northward export of Weddell Sea Deep Water (WSDW) to the Scotia Sea are closely linked to a reduction in the underlying Weddell Sea Bottom Water (WSBW). Zhou et al. (2023) documented a long-term decline in WSBW volume driven by reduced sea-ice formation in the southern Weddell Sea, partly associated with interdecadal wind variability linked to the Interdecadal Pacific Oscillation. This combination of reduced WSBW formation and diminished export of WSDW provides a plausible mechanism for the contraction observed along the SAMBA-West line. Consistent with this interpretation, Biló et al. (2024) reported a (12 ± 5)% weakening in northward AABW transport at 16°N between 2000 and 2020, suggesting that the contraction signal propagates well beyond the South Atlantic to the tropical North. Together, these studies provide multiple, independent lines of evidence linking the contraction observed at SAMBA-West to processes in the Weddell Sea, even though the precise mechanisms and advection pathways remain to be fully understood.

7. Summary and conclusions

In this study, we combined hydrographic and moored observations with a high-resolution numerical simulation to investigate abyssal

variability along the SAMBA-West line. We analyzed the modeled circulation to better characterize how the SAMBA-West line is embedded within the broader abyssal flow of the Argentine Basin, providing essential spatial context for interpreting the observations. Within this framework, and building on the initial assessment of abyssal temperature changes reported by Meinen et al. (2020), we addressed two scientific questions: (1) What is the spatial distribution of the abyssal warming along the SAMBA-West line? (2) What mechanisms drive the observed changes?

The simulation shows that the SAMBA-West array is located in a closed circulation region in the northwestern portion of the Argentine Basin, marked by positive ψ values, where the abyssal circulation over the transect appears strongly influenced by bathymetry. Site BB, in particular, lies at the edge of this large closed circulation region and, in terms of dynamics, seems more closely related to Site C, since both locations are characterized by velocity variability that far exceeds the mean flow, while Sites CC and D exhibit more constant flow characteristics. Water crossing Sites CC, C, and D primarily come from the central part of the basin, whereas at Site BB it appears to come from the southwestern portion of the basin.

Our analysis of the temperature records confirms that the AABW layer continued to warm beyond 2019 and through 2022 at Sites C and D. Despite having fewer CTD profiles, Site CC exhibits a vertical warming structure similar to those sites, reinforcing the spatial coherence of the abyssal warming signal across the eastern portion of the SAMBA-West line. In contrast, Site BB, located at the edge of both the AABW domain and the region of positive ψ, shows elevated temperature variability and no statistically significant long-term trend, likely reflecting its unique position among the assessed sites. These results point to a consistent abyssal warming signal across the eastern portion of the SAMBA-West line.

The heave–spiciness decomposition indicates that heave, rather than spiciness, is the dominant contributor to the abyssal temperature trends along the SAMBA-West line. This implies that vertical displacements of isopycnals are the primary driver of the observed warming. At Sites C, CC, and D, this contraction is expressed as a thinning of the coldest, densest AABW layers, partially compensated by a thickening of the warmer layers above. These changes are consistent with reduced formation or export of AABW to the region.

Although a dedicated study is still required to directly connect the contraction signal of the AABW at the SAMBA-West line to its Weddell Sea source and to fully understand the drivers of this connection, including potential propagation mechanisms such as internal waves (Masuda et al., 2010), several independent lines of evidence support this link. This contraction is consistent with the broader hypothesis that weakened production of dense waters in the Weddell Sea has slowed the abyssal cell of the Atlantic meridional overturning circulation (Zhou et al., 2023; Meredith et al., 2014; Abrahamsen et al., 2019). However, attribution of its drivers remains challenging: data are sparse both at the AABW formation sites and along the pathways that connect them to the SAMBA-West line, leaving interpretations at the level of conjecture, despite the growing evidence for a basin-wide contraction signal.

Taken together, these results provide robust evidence of an ongoing abyssal warming in the Argentine Basin, driven primarily by the contraction of abyssal waters. In this context, the SAMBA-West array emerges as a crucial observational location for tracking these changes, especially given its position at one of the main AABW pathways. Continued and more frequent sampling at this location, through recurrent hydrographic cruises and the deployment of new abyssal moorings, will better capture abyssal water mass changes and deepen our understanding of the mechanisms driving AABW variability and its broader implications for the global climate system. In parallel, dedicated numerical simulations focused on better representing abyssal dynamics and trends are needed to complement the GIGATL6 results and to provide insight into the evolution of abyssal water masses.

CRediT authorship contribution statement

Daniel M.C. Santos: Writing – original draft, Visualization, Software, Methodology, Investigation, Formal analysis, Data curation, Conceptualization. **Tiago C. Biló:** Writing – review & editing, Software, Methodology, Formal analysis, Conceptualization. **Dante C. Napolitano:** Writing – review & editing, Software, Formal analysis, Conceptualization. **Renellys C. Perez:** Writing – review & editing, Funding acquisition, Data curation, Conceptualization. **Jonathan Gula:** Writing – review & editing, Software, Data curation. **Shenfu Dong:** Writing – review & editing, Funding acquisition. **Edmo J.D. Campos:** Funding acquisition. **Olga T. Sato:** Writing – review & editing, Validation, Supervision, Resources, Project administration, Methodology, Funding acquisition, Conceptualization.

Declaration of Generative AI and AI-assisted technologies in the writing process

During the preparation of this work, the authors used ChatGPT to improve the readability and language of the manuscript. After using this tool, the authors reviewed and edited the content as needed and assume full responsibility for the content of the published article.

Declaration of competing interest

The authors declare that they have no known competing financial interests or personal relationships that could have appeared to influence the work reported in this paper.

Acknowledgments

This work was supported by FAPESP, Brazil [2021/09317-3, 2017/09659-6], and financed in part by the Coordenação de Aperfeiçoamento de Pessoal de Nível Superior - Brasil (CAPES) - Finance Code 001. T.C.B., R. P., and S. D. gratefully acknowledge the funding from the NOAA's Global Ocean Monitoring and Observing program (FundRef number 100007298); NOAA's Climate Program Office, Climate Observations and Monitoring, and Climate Variability and Predictability programs under NOFO NOAA-OAR-CPO-2021-2006389 with additional NOAA Atlantic Oceanographic and Meteorological Laboratory support. This research was carried out in part under the auspices of the Cooperative Institute for Marine and Atmospheric Studies, a cooperative institute of the University of Miami and the National Oceanic and Atmospheric Administration (NOAA), cooperative agreement NA 20OAR4320472. T.C.B. also thanks the support provided by the US National Science Foundation (Award# OCE-1949198) and the additional support from the University of Maine's School of Marine Science and the Office of the Vice President for Research. D. C. N. acknowledges support from Région Bretagne, France, the French National Agency for Research through the EUREC4A-OA (ANR-19-JPOC-0004-05) and the CROSSROAD (ANR-21-CE01-0011) projects. J.G. was supported by the French National Agency for Research (ANR) through the project DEEPER (ANR-19-CE01-0002-01). GIGATL simulations were performed using HPC resources from GENCI-TGCC (Grants 2024-A0170112051) and from DATARMOR of "Pôle de Calcul Intensif pour la Mer" at Ifremer, Brest, France. We thank the captains and crew of R/V Puerto Deseado, R/V Alpha Crucis, R/V Maria S. Merian, and R/V Austral who supported our work at sea. We acknowledge the Servicio de Hidrografía Naval (SHN). We acknowledge the Brazilian Navy, SeCIRM, Petróleo Brasileiro S.A. (PETROBRAS), and the Agência Nacional do Petróleo (ANP) for enabling the field campaign of the Brazilian vessels through the Cooperation Term SIGITEC 2018/00451-6 and 2018/00452-2. We thank Marcela Charo for all the help with the processing and quality control of the CTD data. We thank the Instituto Oceanográfico da Universidade de São Paulo.

Appendix A. Supplementary data

Supplementary material related to this article can be found online at https://doi.org/10.1016/j.dsr.2025.104627.

Data availability

CTD and LADCP data from the cruises SAM02 (08/2009) until SAM18 (07/2019) are available at https://www.aoml.noaa.gov/ftp/pub/phod/pub/SAM/hydrographic_data/. The LADCP data of the cruises SAM19 (08/2022) and SAM20 (12/2022) are available at: https://doi.org/10.5281/zenodo.11149277 (Santos et al., 2024c) and https://doi.org/10.5281/zenodo.11108848 (Santos et al., 2024d), respectively. The CTD data of the cruises SAM19 and SAM20 are available at: https://doi.org/10.5281/zenodo.11149213 (Santos et al., 2024a) and https://doi.org/10.5281/zenodo.11148978 (Santos et al., 2024b), respectively. The CTD data of the MSM60 cruise are available at: https://doi.org/10.1594/PANGAEA.915898 (Karstensen, 2020b) and the LADCP data at: https://doi.org/10.1594/PANGAEA.915879 (Karstensen, 2020a). CPIES temperature records from Site C and D are available at: www.aoml.noaa.gov/phod/research/moc/samoc/sam/ (Meinen et al., 2020). CPIES records from Sites AA and BB are available at: https://doi.org/10.5281/zenodo.15365407 (Santos et al., 2025). GEBCO data are available at: https://www.gebco.net/data_and_products/gridded_bathymetry_data/. The source code of the simulation used in this study is available at https://doi.org/10.5281/zenodo.4948523 Gula et al. (2021).

References

Abrahamsen, E.P., Meijers, A.J., Polzin, K.L., Naveira Garabato, A.C., King, B.A., Firing, Y.L., Sallée, J.B., Sheen, K.L., Gordon, A.L., Huber, B.A., et al., 2019. Stabilization of dense antarctic water supply to the Atlantic Ocean overturning circulation. Nat. Clim. Chang. 9 (10), 742–746.

Auclair, F., Benshila, R., Bordois, L., Boutet, M., Brémond, M., Caillaud, M., Cambon, G., Capet, X., Debreu, L., Ducousso, N., Dufois, F., Dumas, F., Ethé, C., Gula, J., Hourdin, C., Illig, S., Jullien, S., Corre, M.L., Gac, S.L., Gentil, S.L., Lemarié, F., Marchesiello, P., Mazoyer, C., Morvan, G., Nguyen, C., Penven, P., Person, R., Pianezze, J., Pous, S., Renault, L., Roblou, L., Sepulveda, A., Theetten, S., Schaefer, A.L., Treillou, S., Valat, S., 2025. Coastal and regional ocean community model. http://dx.doi.org/10.5281/zenodo.15064113.

Becker, J., Sandwell, D., Smith, W., Braud, J., Binder, B., Depner, J., Fabre, D., Factor, J., Ingalls, S., Kim, S., et al., 2009. Global bathymetry and elevation data at 30 arc seconds resolution: SRTM30_ PLUS. Mar. Geod. 32 (4), 355–371.

Biló, T.C., Perez, R.C., Dong, S., Johns, W.E., Kanzow, T., 2024. Weakening of the atlantic meridional overturning circulation abyssal limb in the North Atlantic. In: 2024 Ocean Sciences Meeting. AGU.

Bindoff, N.L., Mcdougall, T.J., 1994. Diagnosing climate change and ocean ventilation using hydrographic data. J. Phys. Oceanogr. 24 (6), 1137–1152.

Campos, E.J., Van Caspel, M.C., Zenk, W., Morozov, E.G., Frey, D.I., Piola, A.R., Meinen, C.S., Sato, O.T., Perez, R.C., Dong, S., 2021. Warming trend in antarctic bottom water in the vema channel in the south atlantic. Geophys. Res. Lett. 48 (19), e2021GL094709.

Carton, J.A., Giese, B.S., 2008. A reanalysis of ocean climate using Simple Ocean Data Assimilation (SODA). Mon. Weather Rev. 136 (8), 2999–3017.

Chidichimo, M.P., Perez, R.C., Speich, S., Kersalé, M., Sprintall, J., Dong, S., Lamont, T., Sato, O.T., Chereskin, T.K., Hummels, R., et al., 2023. Energetic overturning flows, dynamic interocean exchanges, and ocean warming observed in the South Atlantic. Commun. Earth Environ. 4 (1), 10.

Chidichimo, M.P., Piola, A.R., Meinen, C.S., Perez, R., Campos, E.J.D., Dong, S., Lumpkin, R., Garzoli, S., 2021. Brazil Current Volume Transport Variability during 2009–2015 from a long-term moored array at 34.5°S. J. Geophys. Res.: Ocean. 126 (5), e2020JC017146.

Coles, V.J., McCartney, M.S., Olson, D.B., Smethie Jr., W.M., 1996. Changes in Antarctic Bottom Water properties in the western South Atlantic in the late 1980s. J. Geophys. Res.: Ocean. 101 (C4), 8957–8970.

Georgi, D.T., 1981. Circulation of bottom waters in the southwestern South Atlantic. Deep. Sea Res. Part A. Ocean. Res. Pap. 28 (9), 959–979.

Gula, J., Theetten, S., Cambon, G., Roullet, G., 2021. Description of the GIGATL simulations. http://dx.doi.org/10.5281/zenodo.4948523.

Häkkinen, S., Rhines, P.B., Worthen, D.L., 2016. Warming of the global ocean: Spatial structure and water-mass trends. J. Clim. 29 (13), 4949–4963.

Heuzé, C., 2020. Antarctic bottom water and North Atlantic deep water in CMIP6 models. Ocean. Sci. Discuss. 2020, 1–38.

Hogg, N., Biscaye, P., Gardner, W., Schmitz Jr., W.J., 1982. On the transport and modification of Antarctic Bottom Water in the Vema Channel.

Hogg, N.G., Owens, W.B., 1999. Direct measurement of the deep circulation within the Brazil Basin. Deep. Sea Res. Part II: Top. Stud. Ocean. 46 (1–2), 335–353.

Hogg, N.G., Zenk, W., 1997. Long-period changes in the bottom water flowing through Vema Channel. J. Geophys. Res.: Ocean. 102 (C7), 15639–15646.

Johnson, G.C., 2008. Quantifying Antarctic bottom water and North Atlantic deep water volumes. J. Geophys. Res.: Ocean. 113 (C5).

Johnson, G.C., 2022. Antarctic bottom water warming and circulation slowdown in the Argentine Basin from analyses of deep argo and historical shipboard temperature data. Geophys. Res. Lett. 49 (18), e2022GL100526.

Johnson, G.C., McTaggart, K.E., Wanninkhof, R., 2014. Antarctic Bottom Water temperature changes in the western South Atlantic from 1989 to 2014. J. Geophys. Res.: Ocean. 119 (12), 8567–8577.

Johnson, G.C., Purkey, S.G., 2024. Refined estimates of global ocean deep and abyssal decadal warming trends. Geophys. Res. Lett. 51 (18), e2024GL111229.

Karstensen, J., 2020a. Lowered ADCP data during MARIA S. MERIAN cruise MSM60/1. http://dx.doi.org/10.1594/PANGAEA.915879.

Karstensen, J., 2020b. Physical oceanography (CTD) during maria S. Merian cruise MSM60/1. http://dx.doi.org/10.1594/PANGAEA.915898.

Karstensen, J., Speich, S., Asdar, S., Berbel, G.B.B., Branlard, L., Carvalho, A., Chidichimo, M.P., Cotrim da Cunha, L., da Silva Calixto, A., Edsgren, C., Guerrero, R., Hummels, R., Jones, S., Kersale, M., Lebehot, A., Marshall, T., Mohale, N., Rogge, A., Sato, O.T., Schrandt, J., Stöven, T., Sutti Otera, B., 2019. Seamount observatory and SAMOC overturning, cruise no. MSM60, January 04 - February 01, 2017, Cape Town *SouthAfrica* - Montevideo *Uruguay*. pp. 1–46. http://dx.doi.org/10.2312/cr_msm60, URL https://www.tib.eu/de/suchen/id/awi%3A8afb37850edb33cd39ff6bf1a0d55438bac05410.

Li, Z., Chao, Y., McWilliams, J.C., 2006. Computation of the streamfunction and velocity potential for limited and irregular domains. Mon. Weather Rev. 134 (11), 3384–3394.

Masuda, S., Awaji, T., Sugiura, N., Matthews, J.P., Toyoda, T., Kawai, Y., Doi, T., Kouketsu, S., Igarashi, H., Katsumata, K., et al., 2010. Simulated rapid warming of abyssal North Pacific waters. Science 329 (5989), 319–322.

McDonagh, E.L., Arhan, M., Heywood, K.J., 2002. On the circulation of bottom water in the region of the Vema Channel. Deep. Sea Res. Part I: Ocean. Res. Pap. 49 (7), 1119–1139.

Meinen, C.S., Garzoli, S.L., Perez, R.C., Campos, E., Piola, A.R., Chidichimo, M.P., Dong, S., Sato, O.T., 2017. Characteristics and causes of Deep Western Boundary Current transport variability at 34.5°S during 2009–2014. Ocean. Sci. 13 (1), 175–194.

Meinen, C.S., Perez, R.C., Dong, S., Piola, A.R., Campos, E.E.J., 2020. Observed ocean bottom temperature variability at four sites in the northwestern Argentine basin: Evidence of decadal deep/abyssal warming amidst hourly to interannual variability during 2009–2019. Geophys. Res. Lett. 47 (18), e2020GL089093.

Meinen, C.S., Piola, A.R., Perez, R., Garzoli, S., 2012. Deep Western Boundary Current transport variability in the South Atlantic: Preliminary results from a pilot array at 34.5°S. Ocean. Sci. 8 (6), 1041–1054.

Meredith, M.P., Jullion, L., Brown, P.J., Naveira Garabato, A.C., Couldrey, M.P., 2014. Dense waters of the Weddell and Scotia Seas: recent changes in properties and circulation. Philos. Trans. R. Soc. A: Math. Phys. Eng. Sci. 372 (2019), 20130041.

Morozov, E., Frey, D., Campos, E., 2018. Flow of antarctic bottom water in the vema channel. a review. 11, (2), pp. 94–102.

Orsi, A.H., Johnson, G.C., Bullister, J.L., 1999. Circulation, mixing, and production of Antarctic Bottom Water. Prog. Oceanogr. 43 (1), 55–109.

Purkey, S.G., Johnson, G.C., 2012. Global contraction of Antarctic Bottom Water between the 1980s and 2000s. J. Clim. 25 (17), 5830–5844.

Purkey, S.G., Smethie Jr., W.M., Gebbie, G., Gordon, A.L., Sonnerup, R.E., Warner, M.J., Bullister, J.L., 2018. A synoptic view of the ventilation and circulation of Antarctic Bottom water from chlorofluorocarbons and natural tracers. Annu. Rev. Mar. Sci. 10, 503–527.

Qu, L., Thomas, L., Gula, J., 2021. Bottom mixing enhanced by tropical storm-generated near-inertial waves entering critical layers in the Straits of Florida. Geophys. Res. Lett. 48 (15), e2021GL093773.

Ray, R.D., 1999. A global ocean tide model from TOPEX/POSEIDON altimetry: GOT99. 2. National Aeronautics and Space Administration, Goddard Space Flight Center.

Ruan, X., Wenegrat, J.O., Gula, J., 2021. Slippery bottom boundary layers: The loss of energy from the general circulation by bottom drag. Geophys. Res. Lett. 48 (19), e2021GL094434.

Saha, S., Moorthi, S., Pan, H.L., Wu, X., Wang, J., Nadiga, S., Tripp, P., Kistler, R., Woollen, J., Behringer, D., et al., 2010. The NCEP climate forecast system reanalysis. Bull. Am. Meteorol. Soc. 91 (8), 1015–1058.

Santos, D.M.C., Campos, E., Perez, R., Piola, A., Sato, O., 2024a. CTD data - SAM19 cruise. http://dx.doi.org/10.5281/zenodo.11149213.

Santos, D.M.C., Campos, E., Perez, R., Piola, A., Sato, O., 2024b. CTD data - SAM20 cruise. http://dx.doi.org/10.5281/zenodo.11148978.

Santos, D.M.C., Campos, E., Perez, R., Piola, A., Sato, O., 2024c. LADCP data - SAM19 cruise. http://dx.doi.org/10.5281/zenodo.11149277.

Santos, D.M.C., Campos, E., Perez, R., Piola, A., Sato, O., 2024d. LADCP data - SAM20 cruise. http://dx.doi.org/10.5281/zenodo.11108848.

Santos, D.M.C., Campos, E., Perez, R., Piola, A., Sato, O., 2025. CPIES temperature and velocity data - sites AA and BB. http://dx.doi.org/10.5281/zenodo.15365407.

Schubert, R., Gula, J., Capó, E., Damien, P., Molemaker, M.J., Vic, C., McWilliams, J.C., 2025. The ocean flows downhill near the seafloor and recirculates upward above. Nat. Commun. 16 (1), 5873.

Shchepetkin, A.F., McWilliams, J.C., 2005. The regional oceanic modeling system (ROMS): a split-explicit, free-surface, topography-following-coordinate oceanic model. Ocean. Model. 9 (4), 347–404.

Smythe-Wright, D., Boswell, S., 1998. Abyssal circulation in the Argentine Basin. J. Geophys. Res.: Ocean. 103 (C8), 15845–15851.

Solodoch, A., Stewart, A., Hogg, A.M., Morrison, A., Kiss, A., Thompson, A., Purkey, S., Cimoli, L., 2022. How does antarctic bottom water cross the Southern Ocean? Geophys. Res. Lett. 49 (7), e2021GL097211.

Tagliabue, A., Lough, A.J., Vic, C., Roussenov, V., Gula, J., Lohan, M.C., Resing, J.A., Williams, R.G., 2022. Mechanisms driving the dispersal of hydrothermal iron from the northern Mid Atlantic Ridge. Geophys. Res. Lett. 49 (22), e2022GL100615.

Umlauf, L., Burchard, H., 2003. A generic length-scale equation for geophysical turbulence models.

Valla, D., Piola, A.R., Meinen, C.S., Campos, E., 2018. Strong mixing and recirculation in the northwestern Argentine Basin. J. Geophys. Res.: Ocean. 123 (7), 4624–4648.

Valla, D., Piola, A.R., Meinen, C.S., Campos, E., 2019. Abyssal transport variations in the Southwest South Atlantic: first insights from a long-term observation array at 34.5°S. Geophys. Res. Lett. 46 (12), 6699–6705.

Vic, C., Hascoët, S., Gula, J., Huck, T., Maes, C., 2022. Oceanic mesoscale cyclones cluster surface Lagrangian material. Geophys. Res. Lett. 49 (4), e2021GL097488.

Zenk, W., Hogg, N., 1996. Warming trend in Antarctic bottom water flowing into the Brazil Basin. Deep. Sea Res. Part I: Ocean. Res. Pap. 43 (9), 1461–1473.

Zenk, W., Morozov, E., 2007. Decadal warming of the coldest Antarctic Bottom Water flow through the Vema Channel. Geophys. Res. Lett. 34 (14).

Zenk, W., Visbeck, M., 2013. Structure and evolution of the abyssal jet in the Vema Channel of the South Atlantic. Deep. Sea Res. Part II: Top. Stud. Ocean. 85, 244–260.

Zhou, S., Meijers, A.J., Meredith, M.P., Abrahamsen, E.P., Holland, P.R., Silvano, A., Sallée, J.-B., Østerhus, S., 2023. Slowdown of Antarctic Bottom Water export driven by climatic wind and sea-ice changes. Nat. Clim. Chang. 13 (7), 701–709.